



Parallax of Star-forming Region G027.22+0.14

S. B. Bian^{1,2} , Y. Xu¹ , J. J. Li¹, Y. W. Wu^{3,4} , B. Zhang⁵ , X. Chen^{5,6} , Y. J. Li¹ , Z. H. Lin^{1,2}, C. J. Hao^{1,2}, and D. J. Liu^{1,2}

¹ Purple Mountain Observatory, Chinese Academy of Sciences, Nanjing 210033, People's Republic of China; xuye@pmo.ac.cn

² School of Astronomy and Space Science, University of Science and Technology of China, Hefei 230026, People's Republic of China

³ National Time Service Center, Key Laboratory of Precise Positioning and Timing Technology, Chinese Academy of Sciences, Xi'an 710600, People's Republic of China

⁴ National Astronomical Observatory of Japan, 2-21-1 Osawa, Mitaka, Tokyo 181-8588, Japan

⁵ Shanghai Astronomical Observatory, 80 Nandan Road, Shanghai 200030, People's Republic of China

⁶ Center for Astrophysics, Guangzhou University, Guangzhou 510006, People's Republic of China

Received 2021 November 16; revised 2021 November 21; accepted 2021 November 24; published 2022 January 11

Abstract

Using the Very Long Baseline Array, we measured the trigonometric parallax and proper motions toward a 6.7 GHz methanol maser in the distant high-mass star-forming region G027.22+0.14. The distance of this source is determined to be $6.3^{+0.6}_{-0.5}$ kpc. Combining its Galactic coordinates, radial velocity, and proper motion, we assign G027.22+0.14 to the far portion of the Norma arm. The low peculiar motion and lower luminosity of G027.22+0.14 support the conjecture by Immer et al. that low-luminosity sources tend to have low peculiar motions.

Unified Astronomy Thesaurus concepts: Milky Way Galaxy (1054); Star formation (1569); Trigonometric parallax (1713); Interstellar masers (846)

1. Introduction

Reliable distances are requisite to mapping the spiral structure of our Galaxy. However, because of our edge-on view of the Milky Way, obtaining accurate distance measurements to faraway regions is challenging. At optical wavelengths, even for the space satellite Gaia, which has a high, unprecedented astrometric accuracy, interstellar extinction still limits our ability to measure distances to many sources. Meanwhile, Very Long Baseline Interferometry (VLBI) at radio wavelengths has demonstrated the ability to obtain accurate distance measurements for objects up to 20 kpc (Sanna et al. 2017).

Over the last decade, the Bar and Spiral Structure Legacy (BeSSeL) Survey (Brunthaler et al. 2011) and the Japanese VLBI Exploration of Radio Astrometry (VERA) project have measured the parallaxes for more than 200 masers in high-mass star-forming regions (HMSFRs; Reid et al. 2019; VERA Collaboration et al. 2020). Most of those masers are within 5 kpc, which can only depict part of the Milky Way (e.g., Reid et al. 2014, 2019). A better understanding of distant regions requires increasing the accuracy and number of reliable spiral-arm tracers. In this paper, we present a trigonometric parallax measurement of a 6.7 GHz methanol maser toward a distant HMSFR.

2. Observations and Data Analysis

We conducted six separate observations over one year with the National Radio Astronomy Observatory's (NRAO's)⁷ Very Long Baseline Array (VLBA). Table A1 lists the details of the epochs observed. The epochs were selected near the peaks of

the sinusoidal parallax signature in R.A., because the amplitude in decl. was considerably smaller. Three background quasar objects (QSOs) were selected from the VLBA calibrator list on both sides of the maser to provide a reliable interpolation of the fitted planar positional tilt. Two, ≈ 1 hr phase-referenced observations were inserted into three 0.5 hr geodetic blocks during each epoch. We used the same setup for dual-frequency geodetic blocks as described by Xu et al. (2016) to separate and remove ionospheric and tropospheric delays. For the phase-referenced observations, we used four adjacent dual-polarized intermediate-frequency (IF) bands of 16 MHz bandwidth, generating 4000 channels for the methanol maser line in the third IF, yielding a velocity resolution of 0.18 km s^{-1} . In each epoch, we cycled the phase-referenced observations between the maser and each background QSO every 75 s and obtained an on-source integration time of 0.83 hr and 0.25 hr, respectively. Data correlation was performed with the DiFX⁸ software correlator (Deller et al. 2007) in Socorro, New Mexico.

The correlated data were reduced using Astronomical Image Processing System (AIPS) and ParselTongue (Kettenis et al. 2006) scripts. We chose a channel with a strong and compact maser spot as a phase reference to serve as a calibrator for all the maser channels and the background QSOs. Then, we used the AIPS task IMAGR to image the emission in the maser channels and the continuum emission of the QSOs. Finally, we used the AIPS task JMFIT to get the positions of the maser spots and background QSOs by fitting 2D elliptical Gaussian brightness distributions to the images. The positions and brightnesses of the maser source and background QSOs are listed in Table 1.

3. Parallax Estimation

The parallax measurement method for 6.7 GHz methanol masers presented by Reid et al. (2017), which generates an artificial QSO first and then fits the parallax using the artificial

⁷ The National Radio Astronomy Observatory is a facility of the National Science Foundation operated under cooperative agreement by Associated Universities, Inc.

Original content from this work may be used under the terms of the [Creative Commons Attribution 4.0 licence](https://creativecommons.org/licenses/by/4.0/). Any further distribution of this work must maintain attribution to the author(s) and the title of the work, journal citation and DOI.

⁸ DiFX, a software correlator for VLBI, is developed as part of the Australian Major National Research Facilities Programme by the Swinburne University of Technology and operated under license.

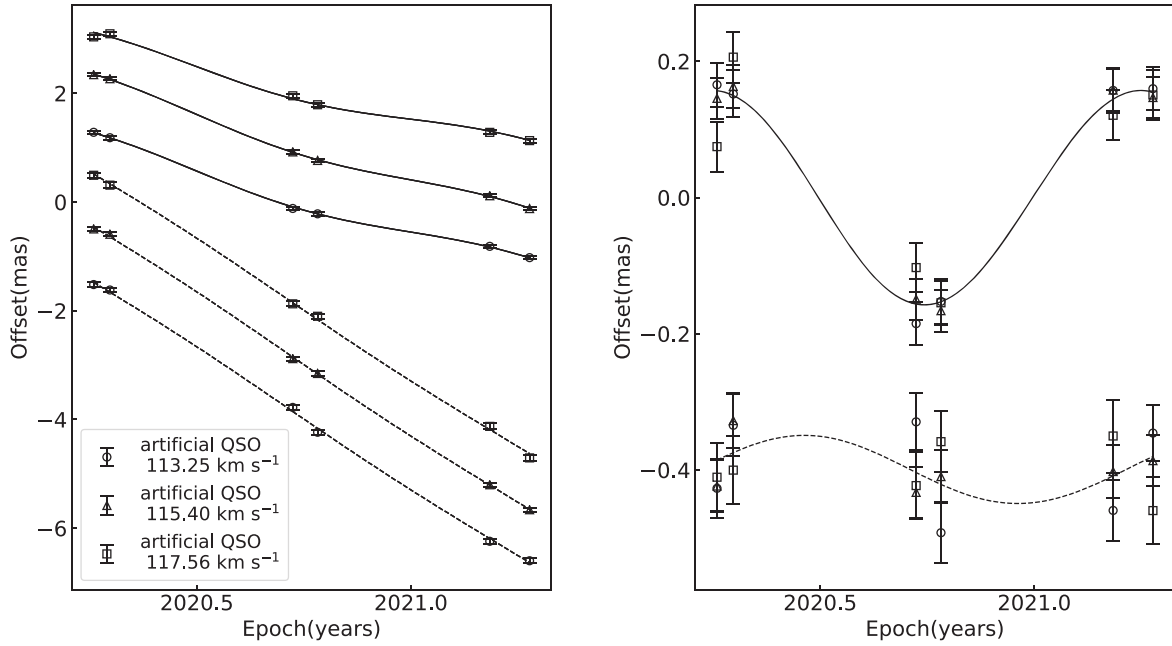


Figure 1. Results from combining the parallax fits for three maser spots. The left panel plots the data and fits of positions changing with time, and the right shows the parallax signatures after proper motions were removed. The best-fitting models in R.A. and decl. are shown as solid dashed lines. Different marks indicate different maser spots as shown in the figure legend.

Table 1
Positions and Brightnesses

Source	R.A. (J2000) (^{hms})	Decl. (J2000) (^{°m})	R.A. _{sep} ([°])	Decl. _{sep} ([°])	Brightness (Jy beam ⁻¹)	V _{LSR} (km s ⁻¹)	NW beam (mas × mas @ °)
G027.22+0.14	18 40 30.5420	−05 01 05.519	8.3	115.40	5.5 × 3.4 @ 178
J1833−0323	18 33 23.90503	−03 23 31.4446	−1.8	1.6	0.055		5.0 × 2.5 @ 0
J1834−0301	18 34 14.07465	−03 01 19.6265	−1.6	2.0	0.051		5.1 × 3.7 @ 11
J1846−0651	18 46 06.30047	−06 51 27.7472	1.4	−1.8	0.043		5.4 × 2.6 @ 1

Note. R.A._{sep}, i.e., $\Delta\text{R.A.}\cos(\text{Dec})$, and Decl._{sep} are the angular separation between the maser and its calibrator in R.A. and in decl., respectively. The maser’s absolute position, peak brightness, size, and position angle, measured from north to east, of the naturally weighted (NW) beam are listed for the first epoch. V_{LSR} is the velocity of the phase-reference channel.

QSO, was improved to only one step as described by Zhang et al. (2019). Zhang et al. (2019) modeled the position of a maser spot relative to multiple QSOs for each epoch as the sum of the maser’s parallax, proper motion, and a planar tilt resulting from ionospheric “wedges.” We used their method for parallax fitting.

We selected three compact maser spots for parallax fitting, their positions measured at each epoch are listed in Table A2. Based on the measured relative positions between the maser spots and QSOs, following Wu et al. (2019), the Markov chain Monte Carlo approach was used to generate marginalized probability distribution functions for all parameters, where all parameters were varied simultaneously. Then, the parallax and proper motions values were obtained by fitting the marginalized distribution functions. The fitting results are shown in Figure 1 and Table A3. Since different maser spots share essentially the same systematic error caused by interferometric propagation delays, we multiplied the parallax formal uncertainty by $\sqrt{3}$, i.e., the root of the number of spots used for parallax fitting. We also averaged the motions of the three maser spots to determine the motions of the central star.

An uncertainty of 5 km s⁻¹ was added in quadrature to the formal uncertainties at the measured distance by considering the typical value of maser motions relative to the central star. The local-standard-of-rest (LSR) velocity we adopted is the median value of the methanol maser emission, which is consistent with the NH₃ molecular line emission from the ATLASGAL survey (Wienen et al. 2012). Table 2 lists the parallax, distance, proper motions, and LSR velocity. A parallax of 0.158 ± 0.014 mas corresponds to a distance of $6.3^{+0.6}_{-0.5}$ kpc with an parallax accuracy of better than 10%. From which, the hosted HMSFR and it is associated arm can be located accurately.

4. Galactic Location

Generally, we assign a maser source to an arm segment using a parallax-based distance estimator (Reid et al. 2016, 2019); i.e., not only by comparing the $(l, b, v)_{\text{src}}$ position of the source with the $(l, b, v)_{\text{arm}}$ loci of arm segments determined primarily from CO and 21 cm Galactic plane surveys, but also by constructing a distance probability density function (PDF), which combines each type of

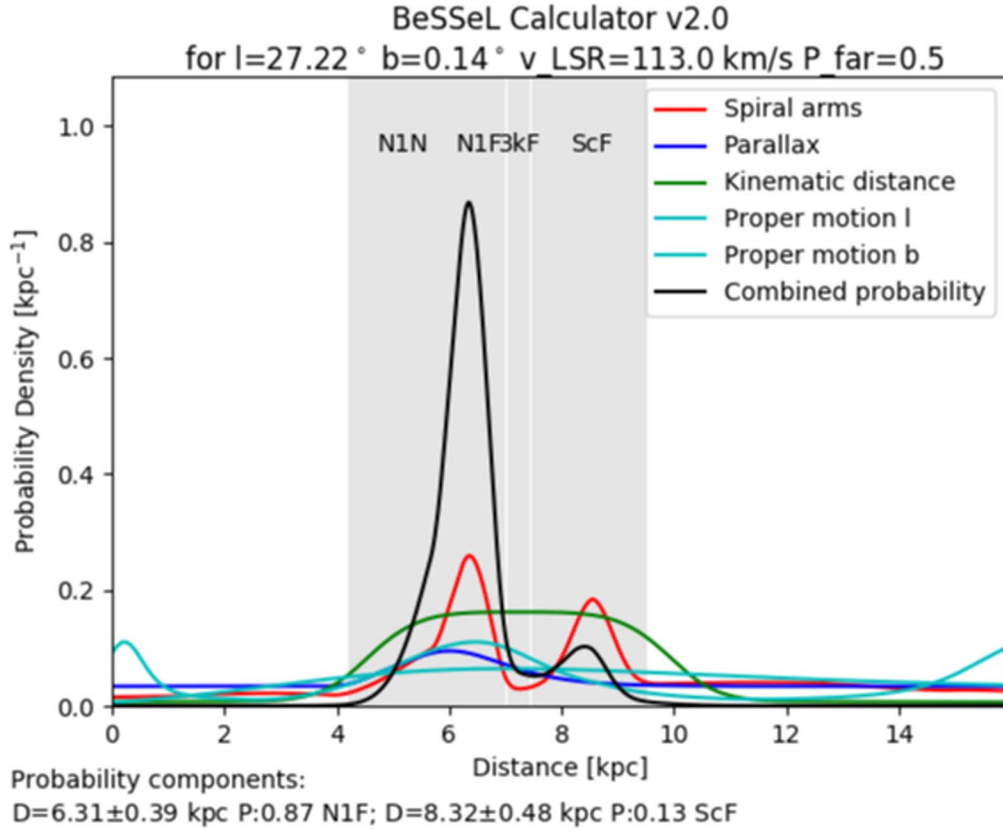


Figure 2. Distance PDF for G027.22+0.14 calculated with a Bayesian distance estimator (Reid et al. 2016, 2019). Each probability is indicated in a differently colored curve (see the legend in the upper-right corner). The name of spiral-arm segments are in short form: N1N/F = Norma arm (near/far); 3kF = 3 kpc arm far; ScF = Scutum arm far. P is the probability of a component.

Table 2
Parallaxes and Proper Motions

Source	π (mas)	D (kpc)	μ_x (mas yr ⁻¹)	μ_y (mas yr ⁻¹)	V_{LSR} (km s ⁻¹)
G027.22+0.14	0.158 ± 0.014	$6.3^{+0.6}_{-0.5}$	-2.21 ± 0.17	-5.08 ± 0.18	$113 (113) \pm 3$

Note. Column 1 gives the Galactic source name/coordinates. Columns 2 through 5 give the parallax, parallax distance, and proper motions in the eastward ($\mu_x = \mu_\alpha \cos \delta$) and northward directions ($\mu_y = \mu_\delta$), respectively. Column 6 lists the LSR velocity determined from the median value of maser emission and that (in parentheses) from $\text{NH}_3(J, K) = (1, 1)$ emission (Wienen et al. 2012).

information in a Bayesian approach, including a spiral-arm model consisting of the parallax measurements, kinematic distances from both LSR velocity and proper motions, Galactic latitude, and the locations of giant molecular clouds with measured parallaxes. The (l, b, v) position of G027.22+0.14 is consistent with both the far side of the Norma arm and the far side of the Scutum arm, as the red curve shows in Figure 2. Its distance PDF (black curve in Figure 2) favors the Norma arm (6.3 kpc), but the Scutum arm (8.3 kpc) may also be a candidate. Our parallax distance of $6.3^{+0.6}_{-0.5}$ kpc resolves this tension, and we assign G027.22+0.14 to the far portion of the Norma arm.

Figure 3 shows the newly measured maser source (green pentagram) superimposed on a map (see Figure 2 in Reid et al. 2019) containing ~ 200 maser sources. From Figure 3, one can see that G027.22+0.14 is located at the far end of the Norma arm, suggesting agreement with the arm width found by Reid

et al. (2019). In the vicinity within 1 kpc, four maser sources were measured and used to fit the model of the Norma arm (Reid et al. 2019). Since those four sources are located at the same side of the Norma arm (red solid line in Figure 3), our measured maser at the other side of the fitted Norma arm indicates that our result agrees with the previous measurements and strengthens the present arm model.

G027.22+0.14 is located along the near-end of the bar, where a large number of HMSFRs are known to exist, and many of which have anomalous peculiar motions (Immer et al. 2019; Xu et al. 2021). Table 3 lists the peculiar motions (U_s, V_s, W_s) for G027.22+0.14 calculated by the methodology given by Reid et al. (2009) with the Galactic parameters and the solar motions of A5 fit by Reid et al. (2019). The peculiar motions in the Galactic rotation, V_s , and toward the north Galactic pole, W_s , are consistent with a typical value of $\lesssim 10 \text{ km s}^{-1}$ (Reid et al. 2019). The uncertainty of U_s (toward

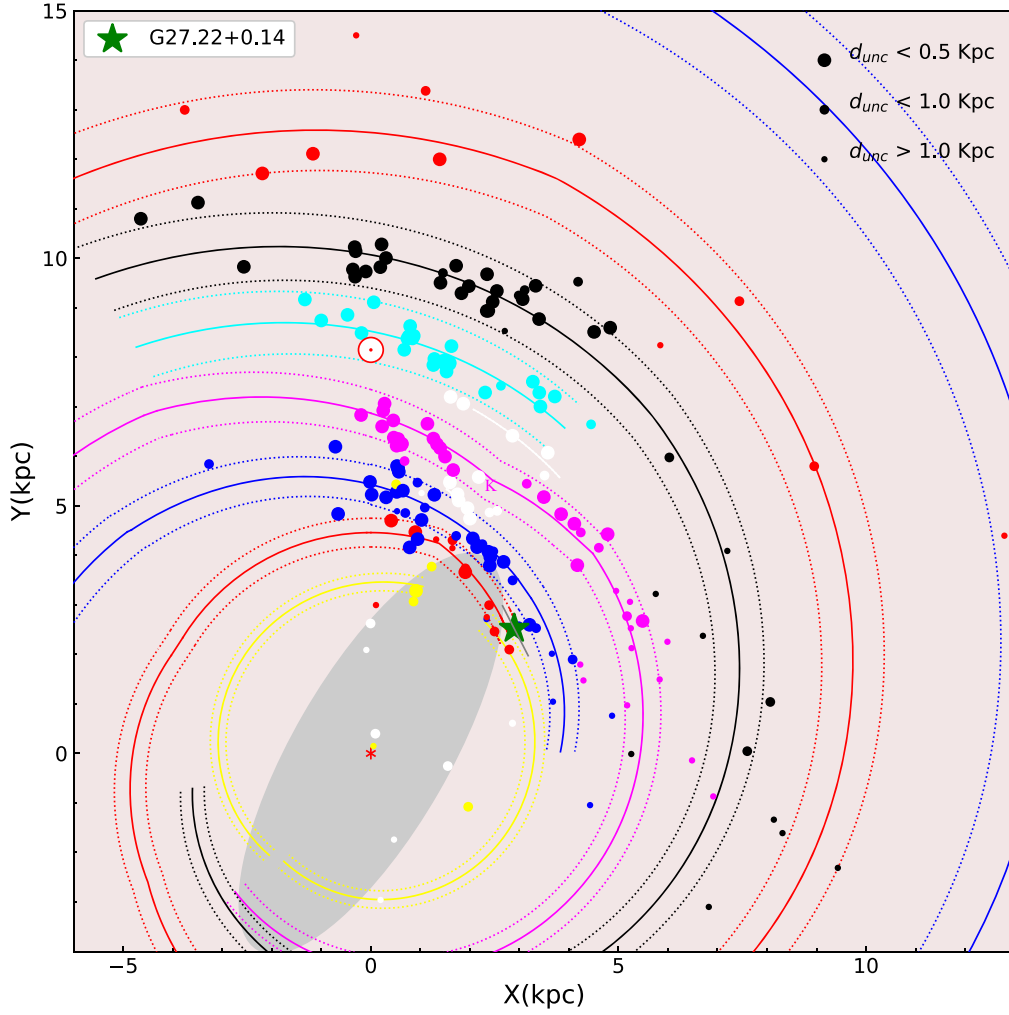


Figure 3. Plan view of the Milky Way from the north Galactic pole following Reid et al. (2019). The background map combines BeSSeL Survey and VERA project results. The green pentagram with a 1σ parallax distance error indicates the source reported in this paper (see the legend in the upper left corner). The locations of maser sources with measured parallaxes are indicated with solid dots. Solid curved lines trace the centers of spiral-arm models from Reid et al. (2019), and the dotted lines enclose 90% of the sources.

Table 3
Peculiar Motions

Source	U_s (km s^{-1})	V_s (km s^{-1})	W_s (km s^{-1})
G027.22+0.14	5 ± 19	4 ± 4	-3 ± 5

Note. The Galactic “Univ” model and solar motions found by Reid et al. (2019) were used to calculate the peculiar motions.

the Galactic center) is too large ($\sim 20 \text{ km s}^{-1}$) to determine whether this source is moving toward the Galactic center or not. However, adopting the definition of whether $|U_s|$ greater or less than 20 km s^{-1} is a high or low peculiar motion from Immer et al. (2019), G027.22+0.14 is likely to be a low peculiar motion source. Immer et al. (2019) found a hint that masers with high peculiar motions are hosted in clouds that are on average more luminous than those of low peculiar motion masers. The bolometric luminosity of G027.22+0.14 from the ATLASGAL clump catalog (Urquhart et al. 2018) was determined using a kinematic distance of 8.0 kpc (far

distance) based on the H I self-absorption technique. However its parallax distance of $6.3^{+0.6}_{-0.5}$ kpc is much less, suggesting its luminosity was over estimated. After correcting for our measured parallax, its bolometric luminosity is $10^{3.8} L_{\odot}$, which is less luminous than every source with a high peculiar motion found by Immer et al. (2019). This adds support for the conjecture by Immer et al. (2019) that low-luminosity sources tend to have low peculiar motions.

This work was supported by the National Natural Science Foundation of China (grant Nos.: 11933011, 11873019), and the Key Laboratory for Radio Astronomy. Y.J.L. was supported by the Natural Science Foundation of Jiangsu Province (grants No. BK20210999).

Appendix

Here, we show the details of the epochs observed (Table A1), positions measured at each epoch (Table A2), and parallax fits with formal uncertainties (Table A3).

Table A1
Details of the Epochs Observed

Program	Source	Epoch 1	Epoch 2	Epoch 3	Epoch 4	Epoch 5	Epoch 6
BB415	G027.22+0.14	2020 Apr 04	2020 Apr 18	2020 Sep 21	2020 Oct 12	2021 Mar 08	2021 Apr 11

Table A2
Positions Measured at Each Epoch

V_{LSR} (km s ⁻¹)	J1833–0323		J1834–0301		J1846–0651	
	Δx (mas)	Δy (mas)	Δx (mas)	Δy (mas)	Δx (mas)	Δy (mas)
Epoch 1						
113.25	-2.884 ± 0.038	32.956 ± 0.059	-4.432 ± 0.039	34.001 ± 0.060	-5.726 ± 0.038	33.857 ± 0.060
115.40	2.115 ± 0.011	-0.497 ± 0.019	0.567 ± 0.015	0.548 ± 0.022	-0.727 ± 0.011	0.404 ± 0.021
117.56	-25.666 ± 0.024	41.809 ± 0.042	-27.213 ± 0.026	42.855 ± 0.043	-28.508 ± 0.024	42.710 ± 0.042
Epoch 2						
113.25	-2.899 ± 0.039	32.926 ± 0.058	-4.327 ± 0.040	34.057 ± 0.058	-5.648 ± 0.042	33.486 ± 0.064
115.40	1.968 ± 0.017	-0.443 ± 0.027	0.540 ± 0.020	0.688 ± 0.028	-0.781 ± 0.024	0.116 ± 0.038
117.56	-25.837 ± 0.030	41.861 ± 0.046	-27.266 ± 0.032	42.992 ± 0.046	-28.586 ± 0.034	42.421 ± 0.053
Epoch 3						
113.25	-4.096 ± 0.035	30.710 ± 0.056	-5.532 ± 0.036	31.649 ± 0.057	-6.753 ± 0.035	31.436 ± 0.057
115.40	0.566 ± 0.010	-2.764 ± 0.018	-0.870 ± 0.014	-1.825 ± 0.021	-2.091 ± 0.011	-2.038 ± 0.022
117.56	-27.195 ± 0.020	39.668 ± 0.036	-28.631 ± 0.023	40.607 ± 0.037	-29.852 ± 0.021	40.394 ± 0.038
Epoch 4						
113.25	-4.368 ± 0.024	30.764 ± 0.043	-5.597 ± 0.029	31.816 ± 0.048	-6.918 ± 0.024	30.859 ± 0.043
115.40	0.301 ± 0.013	-2.754 ± 0.024	-0.928 ± 0.021	-1.702 ± 0.032	-2.248 ± 0.013	-2.660 ± 0.024
117.56	-27.401 ± 0.024	39.494 ± 0.043	-28.630 ± 0.029	40.546 ± 0.049	-29.950 ± 0.024	39.589 ± 0.044
Epoch 5						
113.25	-4.662 ± 0.037	28.490 ± 0.067	-6.092 ± 0.040	29.780 ± 0.071	-7.513 ± 0.037	28.963 ± 0.068
115.40	-0.134 ± 0.011	-5.050 ± 0.023	-1.564 ± 0.020	-3.760 ± 0.033	-2.985 ± 0.012	-4.577 ± 0.025
117.56	-27.785 ± 0.022	37.240 ± 0.044	-29.215 ± 0.028	38.530 ± 0.050	-30.636 ± 0.023	37.713 ± 0.045
Epoch 6						
113.25	-4.768 ± 0.036	27.886 ± 0.058	-6.127 ± 0.037	29.101 ± 0.058	-7.739 ± 0.036	28.442 ± 0.059
115.40	-0.325 ± 0.011	-5.533 ± 0.018	-1.684 ± 0.014	-4.318 ± 0.021	-3.295 ± 0.012	-4.978 ± 0.021
117.56	-27.947 ± 0.021	36.858 ± 0.035	-29.306 ± 0.023	38.073 ± 0.037	-30.918 ± 0.021	37.414 ± 0.037

Table A3
Detailed Results of Parallaxes and Proper Motions of Maser

Background Source	V_{LSR} (km s ⁻¹)	Parallax (mas)	μ_x (mas yr ⁻¹)	μ_y (mas yr ⁻¹)	Δx (mas)	Δy (mas)
Artificial QSO	113.25	0.136 ± 0.025	-1.95 ± 0.05	-5.06 ± 0.06	-4.999 ± 0.038	33.453 ± 0.060
	115.40	0.159 ± 0.016	-2.42 ± 0.04	-5.11 ± 0.06	0	0
	117.56	0.172 ± 0.015	-2.26 ± 0.04	-5.08 ± 0.06	-27.781 ± 0.025	42.306 ± 0.042
	Combined fit	0.158 ± 0.014				
Average			-2.21 ± 0.04	-5.08 ± 0.06		

ORCID iDs

S. B. Bian  <https://orcid.org/0000-0002-7508-9615>
Y. Xu  <https://orcid.org/0000-0001-5602-3306>
Y. W. Wu  <https://orcid.org/0000-0003-3188-5983>
B. Zhang  <https://orcid.org/0000-0003-1353-9040>
X. Chen  <https://orcid.org/0000-0002-5435-925X>
Y. J. Li  <https://orcid.org/0000-0001-7526-0120>

References

Breen, S. L., Ellingsen, S. P., Contreras, Y., et al. 2013, *MNRAS*, **435**, 524
Brunthaler, A., Reid, M. J., Menten, K. M., et al. 2011, *AN*, **332**, 461
Deller, A. T., Tingay, S. J., Bailes, M., et al. 2007, *PASP*, **119**, 318
Immer, K., Li, J., Quiroga-Núñez, L. H., et al. 2019, *A&A*, **632**, A123
Kettenis, M., van Langevelde, H. J., Reynolds, C., et al. 2006, *adass*, **351**, 497
Reid, M. J., Brunthaler, A., Menten, K. M., et al. 2017, *AJ*, **154**, 63
Reid, M. J., Dame, T. M., Menten, K. M., et al. 2016, *ApJ*, **823**, 77

- Reid, M. J., Menten, K. M., Brunthaler, A., et al. 2014, [ApJ](#), **783**, 130
- Reid, M. J., Menten, K. M., Brunthaler, A., et al. 2019, [ApJ](#), **885**, 131
- Reid, M. J., Menten, K. M., Zheng, X. W., et al. 2009, [ApJ](#), **700**, 137
- Sanna, A., Reid, M. J., Dame, T. M., et al. 2017, [Sci](#), **358**, 227
- Urquhart, J. S., König, C., Giannetti, A., et al. 2018, [MNRAS](#), **473**, 1059
- VERA Collaboration, Hirota, T., Nagayama, T., et al. 2020, [PASJ](#), **72**, 50
- Wienen, M., Wyrowski, F., Schuller, F., et al. 2012, [A&A](#), **544**, A146
- Wu, Y. W., Reid, M. J., Sakai, N., et al. 2019, [ApJ](#), **874**, 94
- Xu, Y., Bian, S. B., Reid, M. J., et al. 2021, [ApJS](#), **253**, 1
- Xu, Y., Reid, M., Dame, T., et al. 2016, [SciA](#), **2**, e1600878
- Zhang, B., Reid, M. J., Zhang, L., et al. 2019, [AJ](#), **157**, 200